RSC Advances

ROYAL SOCIETY OF CHEMISTRY

www.rsc.org/advances

Dehydrogenation of propane over PtSn/SBA-15 catalysts: effect of the amount of metal loading and state

Xiaoqiang Fan, Jianmei Li, Zhen Zhao, Yuechang Wei, Jian Liu*, Aijun Duan and Guiyuan Jiang*

State Key Laboratory of Heavy Oil Processing, China University of Petroleum, Beijing, 102249, P. R. China

Author information

Corresponding authors:

* E-mail zhenzhao@cup.edu.cn; Tel: 86-10-89731586; Fax: 86-10-69724721

* E-mail liujian@cup.edu.cn; Tel: 86-10-89732326; Fax: 86-10-69724721

Abstract

A series of PtSn/SBA-15 catalysts with different metal loading amounts were prepared by incipient-wetness impregnation method and their catalytic performances were tested for propane dehydrogenation. The catalysts were characterized by means of XRD, BET, TEM, UV-Vis DRS, O_2-TPO, H_2-TPR, XPS and Raman. The catalytic activity for propane dehydrogenation increases with the increasing of loading amount of metal. And it keeps stable when Pt loading amount reached 1 wt%. It is found that the state of Pt or Sn in the catalysts varies with the changes of metal loading. When the loading of Pt and Sn exceed a certain amount (Pt 1wt% and Sn 2 wt%), the state of Pt and Sn changes apparently with the more oxidative Pt and more reduced Sn. The changes of the state of Pt and Sn influence the catalytic performance of these catalysts. Moreover, the size of PtSn nanoparticles increases with the increasing of Pt and Sn amounts, which also results in the change of the catalytic performance. The Pt_1Sn_2/SBA-15 catalyst shows the highest initial activity, which results from increased amount of active sites, the high dispersion of PtSn nanoparticles and the favorable state of Pt and Sn species.

Keywrds: Propane dehydrogenation, Metal loading, State of Pt and Sn, Catalysts

1. Introduction

Propene is an important raw material for the production of polypropene, acrolein, polyacrylonitrile and acrylic acid. And it is typically obtained by means of steam cracking or fluidized catalytic cracking of naphtha. Due to the uncertain oil price and the growing demand of propylene, the catalytic dehydrogenation of propane has received much attention as an alternative way for producing propylene.[1-4] Especially, how to chemically utilize the low cost propane from shale gas is an urgent and practical issue. The reaction of propane dehydrogenation is an endothermic process, which requires a relatively high temperature and low pressure to obtain high yield of propene. However, high temperature facilitates side reactions such as cracking and coke formation. Therefore, it is the key to develop the catalyst possessing high activity, high stability and high selectivity.

Many efforts have been made to develop catalysts with excellent catalytic properties. The Cr-based catalysts have been widely used for propane dehydrogenation, but the restriction of the Cr-based catalysts is typically hazardous.[5] Some other non-noble metal catalysts, including GaO_x,[6] MoO_x,[7] and VO_x[8] have also been investigated, but they exhibit fast deactivation rates than Pt-based catalatst.[1] Pt shows superior activation ability of paraffinic C-H bonds and low activity to C-C cleavage. Therefore, Pt-based catalysts have been widely used for alkane dehydrogenation reaction owing to their excellent activity.[9-14] However, these catalysts also suffer from deactivation caused by the coke formation and sintering of Pt. The addition of Sn to Pt-based catalyst systems can significantly improve the catalytic activity for the dehydrogenation of propane.[15,16] Usually, the role of Sn is proposed to modify the electronic and geometric properties of Pt.[17-19] Furthermore, support effect[20-22] also influences the catalytic performance of PtSn-based catalysts. The catalyst supports for dehydrogenation of propane have to be thermally stable and limited acidity. And for an optimal distribution of the metallic particles, a relatively large surface area and uniform pore size distribution are preferred. SBA-15 is an appropriate support because of its unique pore architecture. Moreover, its confinement effect is also favourable for the high dispersion of noble metal for supported catalysts.[23,24] Compared with the support effect, the amount of active sites and the state of active sites of different catalysts are more important factors for controlling catalytic reaction performance.[25,26] For instance, it has been reported that the loading amount of Cr had an obvious influence on the catalytic activity for the catalytic dehydrogenation of light alkane over mesoporous Cr_2O_3/Al_2O_3 catalysts with the content of Cr 2–15 wt%.[27] The formation of subsurface Cr (III) species might be the reason for the permanent inactivity. In order to investigate the influence factors on the catalytic performance, PtSn/SBA-15 catalysts with different loading amounts of Pt and Sn were prepared. And the ratios of Pt/Sn for different catalysts keep constant. The results indicate that the size of PtSn nanoparticles and the state of Pt and Sn changed with the increasing of Pt and Sn loading. It can provide us some important information to correlate the catalytic performance and the PtSn/SBA-15 catalysts with different Pt and Sn loading amounts.

2. Experimental

2.1 Catalyst preparation

SBA-15 support was synthesized using triblock copolymer (Pluronic P123) as a template according to the procedure reported in the literature.[28] PtSn/SBA-15 catalysts with different loading amouonts of Pt and Sn were prepared by incipient-wetness impregnation method. $SnCl_4 \cdot 5H_2O$ and $H_2PtCl_6 \cdot 6H_2O$ precursors were dissolved in deionized water to form a solution and powder SBA-15 was impregnated in the solution. After that, the mixture was sonicated for 30 min and dried at 25 °C for 24 h. After being completely dried, the catalysts were calcined at 500 °C for 4 h. The nominal compositions of these catalysts were 0.3, 0.5, 1, 2, and 3 wt% Pt with a constant Pt/Sn ratio of 1/2. The SiO_2 supported PtSn catalyst was also prepared by impregnation method.

2.2 Catalyst characterization

Nitrogen adsorption/desorption isotherms at -196 °C were recorded using a Micromeritics TriStar II 3020 porosimetry analyzer. The samples were degassed at 300 °C for 8 h prior to the measurements.

Low-angle X-ray diffraction (XRD) patterns were collected in a 2θ range from 0.7 to 10° with a step size of 0.02° on a SIEMENS D5000 diffratometer. Wide-angle XRD patterns were obtained by a powder X-ray diffractometer (Shimadzu XRD 6000) using Cu Kα (λ= 0.15406 nm) radiation with a Nickel filter operating at 40 kV and 40 mA in the 2θ range of 20-80 ° at a scanning rate of 4 °/min.

Transmission electron microscopy (TEM) images were taken on JEOL JEM 2100 electron microscope equipped with a field emission source at an acceleration voltage of 200 kV. The TEM samples were sonicated and well suspended in ethanol. Drops of the suspension were applied and after drying the fine particles were well dispersed on a copper grid coated with carbon.

Fourier-transform infrared spectra (FT-IR) were collected on a FTS-3000 IR instrument. The samples were mixed with KBr (Sample: KBr=1:100, mass ratio) and pressed into pellets. The spectra were collected in the range of 4000-400 cm^{-1} and KBr was used as background.

The UV-Vis diffuse reflectance spectroscopy (UV-Vis DRS) experiments were performed on a UV-Vis spectrophotometer (Hitachi U-4100) with the integration sphere diffuse reflectance attachment.

X-ray photoelectron spectra (XPS) were recorded on a Perkin-Elmer PHI-1600 ESCA spectrometer using Mg Kα (hv=1253.6 eV, 1 eV=1.603×10^{-19} J) X-ray source. The binding energies were calibrated using C1s peak of contaminant carbon (BE = 284.6 eV) as an internal standard.

Temperature-programmed reduction with H_2 (H_2-TPR) measurements were performed in a conventional flow apparatus. 100 mg sample was pretreated under air atmosphere by calcination at 300 ^{o}C for 1 h and subsequently cooled to 30 ^{o}C. Afterwards, 10 % H_2/Ar flow (40 mL/min) was passed over the catalyst bed while the temperature was ramped from 30 to 800 ^{o}C at a heating rate of 10 ^{o}C/min. The hydrogen consumption signal was monitored by a TCD. Before the outlet gases entering the TCD, a cooling trap and a filter packed with molecular sieve 5A (60-80 meshes) were used to remove H_2O and CO_2.

Temperature-programmed oxidation with O_2 (O_2-TPO) was measured in a conventional flow apparatus. 0.1 g sample was placed in a quartz reactor and then heated up to 650 ^{o}C in a 5%O_2/Ar.

Raman spectra were performed on a Renishaw inVia Reflex Raman spectrometer with a 244 nm laser at room temperature under ambient conditions.

2.3 Catalytic activity measurements

The activity measurements for propane dehydrogenation were carried out in a conventional quartz tubular micro-reactor. The catalyst (mass 0.2 g) was placed in the center of the reactor. Before the reaction, the catalyst was reduced with 10% H_2/Ar at 500 ^{o}C for 4 h. Reaction conditions were as follows: 590 °C for reaction temperature, atmospheric pressure, C_3H_8/Ar=1/3 (molar ratio) and the propane weight hourly space velocity (WHSV) is 2.2 h^{-1}. The reaction products were analyzed with an online SP-2100 gas chromatography. An aluminum column was used for the separation of CH_4, C_2H_4, C_2H_6, C_3H_6, and C_3H_8. The conversion of propane and selectivity of propene were defined as follows:

$$\text{Conversion of propane (\%)}=\frac{\text{Content of propane in feedstock - content of propane in product}}{\text{Content of propane in feedstock}}\times 100$$

$$\text{Selectivity to propene (\%)}=\frac{\text{Content of propene in product}}{\text{Content of propane in feedstock - content of propane in product}}\times 100$$

The intrinsic activity of the catalyst was based on the TOF value, which was defined as the ratio of the molar amount of product to the molar amount Pt metal. The catalyst (mass 0.15 g) with particle diameter <40 μm was placed in the center of the reactor. Before the reaction, the catalyst was reduced with 10% H_2/Ar at 500 ^{o}C for 4 h. The reaction was carried out at 500 ^{o}C with propane flow of 6 ml/min.

3. Results and discussion

3.1 Characterization

3.1.1. XRD results

To investigate the geometrical regularity of mesopores after loading Pt and Sn on SBA-15, the low-angle XRD measurements were carried out and the patterns are shown in Figure 1A. The SBA-15 support shows well-resolved peaks with a sharp peak at 2θ ranged from 0.5 to 2.5°, associated with (100), (110), and (200) reflections of P6mm symmetry. After loaded with Pt and Sn, SBA-15 in the PtSn/SBA-15 samples shows little change, indicating the hexagonal mesostructure is intact after loading metal. The corresponding lattice spacings (d_{100}) and unit-cell parameters (a_0) are listed in Table 1. It can be observed that the d_{100} and a_0 after loading Pt and Sn are quite similar to SBA-15, indicating no significant alteration symmetry of pore structure for PtSn/SBA-15 catalysts. The low-angle XRD results indicate that even with high loading amount of Pt and Sn (Pt 3 wt%), the catalysts can keep the high mesoporous structure of the SBA-15 support.

XRD patterns recorded in the wide-angle domain for these materials are shown in Figure 1B. The broad peak at 2θ of 23.5^{o} is a typical reflection of amorphous silica. Besides the characteristic pattern of SBA-15, the XRD reflections at 2θ of 39.8^{o}, 46.2^{o}, 67.4^{o}, 81.4^{o} and 85.7^{o} can be attributed to (111), (200), (220), (311) and (222) inter planar spacings of the cubic Pt metal structure, respectively.[29] And the characteristic peaks of Pt become more narrow and sharpe with the increasing of the amount of Pt, indicating the gradual increase of Pt crystallite size. The average sizes of Pt crystallites (d_{XRD}) were estimated from the XRD peaks by Scherrer equation and the results are shown in Table 1. The average Pt crystallite size in PtSn/SBA-15 catalysts shows a clear dependence on Pt content, with larger particles formed at higher loading. It can be seen that the d_{XRD} of $Pt_{0.3}Sn_{0.6}$/SBA-15 is about 12.8 nm, and it increases to

38.8 nm of Pt_3Sn_6/SBA-15 catalysts, indicating the dispersion of Pt is significantly higher than that of low Pt loaded catalysts.

As shown in Figure 1B, at low metal loading (Pt<2 wt%) of PtSn/SBA-15 catalysts, No obviously XRD diffraction peaks of Sn or SnO_x were detected. When the loading amount of Pt reached 3 wt%, the peaks at 2θ of 33.9^o and 51.7^o appeared, which indexed to (101) and (211) reflections of SnO_2.[30] For the low loading catalysts, the absence of these XRD diffractions is probably due to the high dispersion of SnO_2 or the formation of amorphous SnO_x phases.

3.1.2. Nitrogen adsorption-desorption measurements

The textural properties of the calcined catalysts were investigated by nitrogen adsorption-desorption and the corresponding isotherms and pore size distributions are shown in Figure 2. As shown in Figure 2A, SBA-15 exhibits isotherm of type IV with hysteresis loops of type H1. It indicates that the highly ordered mesoporous SBA-15 solids have a narrow pore size distribution of the cylindrical channels, which is in good agreement with the results obtained by low-angle XRD. Likewise, it is noticed that PtSn/SBA-15 samples display the isotherms very similar in shape to SBA-15, indicating that these catalysts retain the initial texture of SBA-15. The pore size distribution curves, as shown in Figure 2B, display pore size with high uniformity and show that the pore size nearly keep unchanged, indicating that these catalysts essentially retain the initial texture of the SBA-15 support, as already suggested by low-angle XRD.

On the basis of the adsorption/desorption isotherms, the textural properties were calculated by specific algorithms and they are shown in Table 1. Compared with the SBA-15, the BET surface area of $Pt_{0.3}Sn_{0.6}$/SBA-15 catalyst decreases from 750.6 $m^2 \cdot g^{-1}$ to 707.5 $m^2 \cdot g^{-1}$ after loading of Pt and Sn, and it further decreases with the increasing loading amount of Pt and Sn. Meanwhile, the mesopore volume decreases from 1.2 to 0.99 $cm^3 \cdot g^{-1}$ with the increasing of metal loading amount. These PtSn/SBA-15 catalysts display narrow pore size distributions with the maxima centered at 7.4-7.6 nm for different amounts of metal loading, slightly lower than the maxium at 7.8 nm of SBA-15. It indicates that SnO_x are dispersed in the mesopores of SBA-15.

3.1.3. TEM images

To investigate the morphology of PtSn and to provide evidence on their distribution, TEM analyses were carried out. Figure 3 shows the TEM images of SBA-15 and PtSn/SBA-15 catalysts. SBA-15 sample (Figure 3a) exhibits highly ordered mesoporous structure composed of cylindrical mesochannels with a narrow size distribution, which is in good agreement with the results of N_2 physisorption. After loading Pt and Sn metals, SBA-15 support in PtSn/SBA-15 catalysts (Figure 3b-f) still keeps highly ordered mesoporous structure, indicating high stability of SBA-15 support. Meanwhile, there are some nanoparticles confined in the mesopores appeared in Figure 3b-f, which is assigned to PtSn nanoparticles. It can be seen that the density of the nanoparticles increase with the increasing of Pt and Sn loading. For $Pt_{0.3}Sn_{0.6}$/SBA-15, $Pt_{0.5}Sn_1$/SBA-15 and Pt_1Sn_2/SBA-15 catalyst, although the size of the nanoparticles increases, no large aggregates of the metals on the external surface of SBA-15 were observed. It indicated a good dispersion and uniformly distributed throughout the pores of PtSn nanoparticles. This confirms that the formation of highly dispersed metal nanoparticles confined within the channels of SBA-15 for the three catalysts. The confined effect of SBA-15 has been proved to stabilize the nanoparticles and thus inhibits the sintering of nanoparticles,[31] which can improve the stability of the catalysts during the propane dehydrogenation reaction. When the amount of Pt loading exceeds 2 wt%, some large nanoparticles (> 50 nm) appeared on the external surface of SBA-15 support. It is well known that the reaction of propane dehydrogenation is insensitive to the structure of the platinum particles. That is, such reactions are independent of the platinum particle size or crystallographic plane exposed.[32,33] As the amount of active sites is closely related to catalytic activity, small particles are preferred. However, undesired side reactions that occur during propane dehydrogenation, such as hydrogenolysis, isomerization, and coke formation, are sensitive to the structure of the platinum particles.[34,35] Accordingly, the size of PtSn nanoparticle has influenced on the catalytic performance for propane dehydrogenation. Therefore, the catalytic performances for these PtSn/SBA-15 catalysts may be affected by the size of PtSn nanoparticles.

For Pt_3Sn_6/SBA-15 catalyst, SnO_2 nanocrystals appeared indicating the separation of Pt and Sn on this catalyst. To confirm the distributions of Pt and Sn on Pt_3Sn_6/SBA-15 catalyst, HAADF-STEM experiment combined with EDS element-mapping analyses were carried out and the results are shown in Figure 3g. Pt element is mainly dispersed on the nanoparticles, while Sn element is dispersed not only on the nanoparticles but also on the support. The separation of Pt and Sn species and the formation of SnO_2 nanocrystals are unfavorable for the catalytic activity in propane dehydrogenation reaction.

3.1.4 Raman spectra

Figure 4 shows the Raman spectra of SBA-15 and PtSn/SBA-15 catalysts in the 100-1400 cm^{-1} range. The Raman spectra of SBA-15 resemble those of published visible Raman spectra.[36] As shown in Figure 4, the D_1 and D_2 features at 494 and 609 cm^{-1} are assigned to symmetric O-Si-O motions of vibrationally isolated four-membered rings of SiO_4 tetrahedra and to breathing motions of three-membered rings of SiO_4 tetrahedra, respectively.[37] The combined feature at around 800 and 830 cm^{-1} is assigned to the transverse (TO) and longitudinal (LO) optical components of network motions, respectively. And the band at 976 cm^{-1} is assigned to the Si-OH stretching of free surface silanols.[38] For the low loading PtSn/SBA-15 (Pt<1 wt%) catalysts, with the increasing the amount of metal loadings, the Raman spectra is similar to that of SBA-15 and the intensity of the peaks decreases due to the increasing of metal loading. But for Pt_2Sn_4/SBA-15 and Pt_3Sn_6/SBA-15 catalysts, the intensity of the peaks corresponding to SBA-15 decrease dramatically and some new peaks appear. According to the literature, PtO_2 possesses Raman feature at 504 (A_{1g}) and 545 cm^{-1} (E_g)[39] and metallic Pt is not Raman-active. Therefore, the bands at 504 and 545 cm^{-1} for Pt_2Sn_4/SBA-15 and Pt_3Sn_6/SBA-15 catalysts is assigned to A_{1g} and E_g vibrational modes[40] of PtO_2. The Pt species in Pt_2Sn_4/SBA-15 and Pt_3Sn_6/SBA-15 catalysts exist in the form of both metallic Pt and oxidative Pt species. And the absence of these features of low metal loading (Pt< 1 wt%) PtSn/SBA-15 catalysts indicate the Pt species exist in the form of metallic Pt, as supported by the XRD results. For Pt_2Sn_4/SBA-15 and Pt_3Sn_6/SBA-15 catalysts, the bands at 625 and 755 cm^{-1} appear, which correspond to A_{1g} and B_{2g} symmetry modes of nanocrystallite SnO_2.[41]

According to the Raman characterization, it can be found that Pt and Sn species may exist in different forms with the changing of metal loading. The increasing of Pt amount results in the formation of oxidative Pt species in PtSn/SBA15 catalysts, while the increasing of Sn may lead to little change on the state of Sn species.

3.1.5. UV-Vis DRS spectra

UV-Vis DRS is a sensitive and convenient tool, which is widely used to detect the coordination states of the transition metal ions. Figure 5 shows the UV-Vis absorption spectra of SnO_2 and PtSn/SBA-15 catalysts. The SnO_2 shows two absorption bands with maximum intensities at 240 and 285 nm. The former band is assigned to the O→Sn LMCT (ligand to metal charge transfer) of Sn in an octahedral (O_h) coordination, and the latter one is the electron transition from valence band to conduction band of bulk SnO_2 crystal. [42] For the PtSn/SBA-15 catalysts with the amount of Sn 0.06 and 0.1 wt%, two absorption bands at 216 and 240 nm are observed. The band at 216 nm is ascribed to the O→Sn LMCT of Sn in tetrahedral (T_d) environment. The appearance of this band indicates that Sn isomorphously substitutes in the silica framework. With the increasing of Sn loading, the intensity of the band at 240 nm increases, indicating that the more Sn species are present in an O_h coordinate environment and more SnO_2 nanocrystallites are formed. It can be seen that all of the PtSn/SBA-15 catalysts do not show an apparent peak at 285 nm, which implies that no bulk SnO_2 was detected and the Sn species mainly exist in the form of oxidative Sn nanocrystallites.

The results of UV-Vis DRS indicate that the Sn species exist in the form of oxidized Sn in all PtSn/SBA-15 catalysts. And with the increasing of Sn loading, the proportion of framework Sn species decreases and the proportion of nanocrystallite Sn species increases, which results in the formation of reflection peaks of SnO_2 in XRD pattern of Pt_3Sn_6/SBA-15.

3.1.6. XPS results

To examine the electronic properties of the surface elements, PtSn/SBA-15 catalysts were studied by XPS, and the results are shown in Figure 6 and Table 2. Figure 6A shows the Pt 4f XPS spectra of PtSn/SBA-15 catalysts. For $Pt_{0.3}Sn_{0.6}$/SBA-15 catalyst, the binding energies of 71.5 and 74.4 eV have been assigned to Pt^0. It can be seen that only metallic Pt species are present on

$Pt_{0.3}Sn_{0.6}$/SBA-15 and $Pt_{0.5}Sn_1$/SBA-15 catalysts. When the loading amount of Pt is 1 wt%, there is a new peak appeared at the binding energy of 78.4 eV which is assigned to Pt^{4+} species.[43] The appearance of this peak indicates that both metallic and oxidative Pt species are present on PtSn/SBA-15 catalysts with Pt loading exceeding 1wt%. And the proportion of the Pt^{4+} species increases with the increasing of Pt loading. The XPS spectra were used to estimate the amount of Pt^0 and Pt^{4+} in each sample and the results are presented in Table 2. The contents of Pt^0 in PtSn/SBA-15 catalysts gradually decrease and it becomes 80.6% for Pt_3Sn_6/SBA-15 catalyst. The gradually increase of Pt^{4+} species for PtSn/SBA-15 catalysts with the increasing of Pt loading may results in a negative effect for propane dehydrogenation reaction. There are some possible reasons for the high content of Pt oxidative states: one reason is the existing of the unsaturated bond. The surface atoms of small size Pt nanoparticles (NPs) show strong ability to donate electronics so that O_2 molecules are adsorbed on the surface Pt atoms, which will result in the formation of Pt^{4+}.[43] However, in our PtSn/SBA-15 system, the size of the Pt NPs increases with the increasing of the amount of Pt. So the increasing of Pt^{4+} species caused by the size effect may be not the main reason. The other one is the interaction of Pt and Sn or Pt and support. This is the main reason for our system. Due to the different radius of Pt^{n+} and Sn^{n+}, the lattice defects are formed in the PtSn/SBA-15 catalyst, which leads to more Pt^{4+} with increasing Pt content. Moreover, the size of PtSn NPs increases with the increasing of metal loading, which will influence the interation of Pt and Sn or Pt and support.

Figure 6B shows the XPS spectra corresponding to the Sn $3d_{5/2}$ level of the PtSn/SBA-15 catalysts. A slight shift to low binding energy is displayed from Pt_3Sn_6/SBA-15 to $Pt_{0.3}Sn_{0.6}$/SBA-15 catalyst. It has been reported that alloying with Pt might cause the shift.[44] It is indicated that the alloying degree of Sn species increased with the increasing of Sn loading amount. The deconvolution of the spectra yielded four peaks at 485.4, 486.3, 487.3 and 488.6 eV, representative of the different types of tin species. The Sn $3d_{5/2}$ at 485.4 eV is assigned to Sn^0 in the Pt-Sn alloy. The peaks at 486.3 and 487.3 eV are corresponded to oxidized Sn i.e. Sn^{2+} and Sn^{4+}, respectively. And the peak at 488.6 eV is attributed to Sn species bound to the support (Sn-s).[45] The quantitative analyses for XPS are shown in Table 2. Most of Sn species are characteristic of oxidized Sn species. Moreover, the contents of Sn^0 species at all PtSn/SBA-15 catalysts are similar. The gradually decreasing of Sn-s species with the increasing of metal loading amount in PtSn/SBA-15 catalysts indicates the interaction of Sn species and support became weak. The results of XPS indicates that with the increasing of metal loading, the interations of Pt and Sn, Pt (Sn) and support change due to the effect of PtSn NPs size.

3.1.7. H_2-TPR results

The states of the metals and the interactions of the metal (oxides) components among themselves and with the supports were investigated by H_2-TPR. The H_2-TPR profiles of the PtSn/SBA-15 catalysts are presented in Figure 7. The $Pt_{0.3}Sn_{0.6}$/SBA-15 catalyst shows three reduction peaks at about 348 (peak I), 385 (peak II) and 550 °C (peak III). And with the increasing of the amount of metal loading, the intensity of the reduction peaks increases, indicating more Pt and Sn species were reduced. When the amount of Pt loading is 2 wt%, a new reduction peak at about 250 °C (peak IV) appeared. And the reduction temperature of peak I shifts towards low temperature, which reduced to 317 °C for Pt_3Sn_6/SBA-15 catalyst. In general, the signal at 250 °C can be assigned to the reduction of Pt oxide species, whereas the high-temperature peaks (peak II and peak III) are ascribed to the partial reduction of Sn^{4+} to Sn^{2+} and Sn^{2+} to Sn^0, respectively.[46] Furthermore, most of Pt species can be reduced to Pt^0

during the course of TPR experiment, whereas the reducibility of Sn depends on the extent of interactions between the tin species and the support.[47] The absence of peak IV on $Pt_{0.3}Sn_{0.6}$/SBA-15 and $Pt_{0.5}Sn_1$/SBA-15 indicates that the Pt species in these catalysts exist in the form of metallic state, which is coincidence with the Raman and XRD results. For Pt_1Sn_2/SBA-15 catalyst, the peak IV appeared with low intensity, indicating the existence of Pt oxide. For Pt_2Sn_4/SBA-15 and Pt_3Sn_6/SBA-15 catalysts, the reduction peak of Pt oxide species (peak IV) became apparent, which demonstrated the more oxidative Pt species with the increasing of Pt loading amounts. It is well-known that the state of Pt in bimetallic Pt-Sn catalyst has remarkable influence on the catalytic properties. The existence of oxidative Pt species may result in a decrease of the activities for propane dehydrogenation. Therefore, it is concluded that the increasing of the loading amount of Pt and Sn may be unfavorable for the catalytic performance. The peak I is usually ascribed to the conjunct reduction of Pt and Sn species.[48] The peak decreases from 348 to 317 ^{o}C in PtSn/SBA-15 catalysts, indicating the weakening of interation of Pt and Sn species with the increasing of Pt and Sn loading. An overview of the TPR profile of PtSn/SBA-15 catalyst indicates that the increasing of Pt and Sn loading amounts results in some changes: the state of Pt species and the interaction of Pt and Sn species.

3.2. Catalytic performance for propane dehydrogenation

In order to investigate the role of SBA-15 in the propane dehydrogenation reaction, The SiO_2-supported PtSn catalyst with Pt loading amount of 0.5 wt% was prepared. Table 3 shows the catalytic performances of propane dehydrogenation over PtSn catalysts supported on SBA-15 and SiO_2. It can be seen that both bare SBA-15 and bare SiO_2 hardly show difference on propane conversion. But the catalytic performances over $Pt_{0.5}Sn_1$/SBA-15 and $Pt_{0.5}Sn_1$/SiO_2 have large differences.

$Pt_{0.5}Sn_1$/SBA-15 catalyst shows initial propane conversion of 49.5% while $Pt_{0.5}Sn_1/SiO_2$ of 33.9%. After 6h for the reaction the conversion of propane becomes 32.8% ($Pt_{0.5}Sn_1$/SBA-15) and 19.5% ($Pt_{0.5}Sn_1/SiO_2$), respectively. The reasons for the differences may be that SBA-15 has larger surface area and pore volume than SiO_2, which may be favorable for the dispersion of the actives. Moreover, SBA-15 unique pore architecture makes it very attractive as host for the confinement and stabilization of Pt nanoparticles, which can better maintain their dispersion.[23] Compared with $Pt_{0.5}Sn_1/SiO_2$, $Pt_{0.5}Sn_1$/SBA-15 shows higher propane conversion and considerable propene selectivity.

SBA-15 supported PtSn catalysts with different metal loading amounts were tested for propane dehydrogenation for 6 h. Figure 8 exhibits the catalytic performances of the different catalysts. The conversions of propane on PtSn/SBA-15 catalysts are shown in Figure 8A. The bare SBA-15 shows the conversion of propane is below 1%. The conversion of propane may be due to the thermal decomposition at high temperature (590 ^{o}C), which demonstrates that pure SBA-15 itself is inactive. For $Pt_{0.3}Sn_{0.6}$/SBA-15 catalyst, the initial propane conversion is 46.5% and after reaction for 6 h it becomes 32.8%. With the increasing of Pt and Sn loading amounts, the initial conversion of propane over PtSn/SBA-15 catalysts increases. For example, the initial propane conversions for $Pt_{0.5}Sn_1$/SBA-15 and Pt_1Sn_2/SBA-15 catalysts are of 49.5% and 54.2%, respectively. The increase of conversions may result from the increasing of the active sites due to the increase of metal loading amount. Meanwhile, the catalytic stabilities of the both catalysts are similar with that of $Pt_{0.3}Sn_{0.6}$/SBA-15 catalyst, which shows the final propane conversion of 34.1 ($Pt_{0.5}Sn_1$/SBA-15) and 38.2% (Pt_1Sn_2/SBA-15), respectively. Furthermore, there are significant differences among the PtSn/SBA-15 catalysts for the propane conversion and catalytic stability.

Although the metal loadings of Pt_2Sn_4/SBA-15 and Pt_3Sn_6/SBA-15 catalysts are higher than that of Pt_1Sn_2/SBA-15 catalyst, the initial conversions of propane are lower than that of Pt_1Sn_2/SBA-15 with the conversions of propane 51.0 and 52.8% for Pt_2Sn_4/SBA-15 and Pt_3Sn_6/SBA-15 catalysts, respectively. And Pt_2Sn_4/SBA-15 and Pt_3Sn_6/SBA-15 catalysts show higher stabilities than the others in our experiments, which shows finial conversion of 39.1 (Pt_2Sn_4/SBA-15) and 40.0% (Pt_3Sn_6/SBA-15). Figure 9 shows the relationship between catalytic performance and Pt loading amount. The propane conversion increases with the increasing of metal loading and then it keeps steady with high metal loading (Pt exceeds 1 wt%). It is interesting to find that the initial propane conversion nonlinearly increases with the metal loading and the stabilities of these PtSn/SBA-15 catalysts are also not the same.

Moreover, as shown in Figure 8B, the selectivity of propene on these catalysts shows similar trends and all beyond to 98% during the reaction procedure. Figure 8B shows that, comparing with $Pt_{0.3}Sn_{0.6}$/SBA-15, $Pt_{0.5}Sn_1$/SBA-15 and Pt_1Sn_2/SBA-15 catalysts, the selectivity of propene shows little increase on Pt_2Sn_4/SBA-15 and Pt_3Sn_6/SBA-15 catalysts, suggesting that the enhanced stabilities over these samples may be not from the slower deactivation caused by the side reactions.

The catalytic performances in terms of turn-over frequency were calculated and the results are shown in Table 4. The TOFs decrease with the increasing of metal loading amount. It should be noted that the calculated TOF (5 min) for $Pt_{0.3}Sn_{0.6}$/SBA-15 and $Pt_{0.5}Sn_1$/SBA-15 catalysts are much higher than those of Pt_2Sn_4/SBA-15 and Pt_3Sn_6/SBA-15, which indicates the low efficiency of Pt on high loading amount catalysts. Moreover, the TOF of $Pt_{0.3}Sn_{0.6}$/SBA-15 catalyst decreases from 5.88 s^{-1} (5 min) to 5.24 s^{-1} (60 min), indicating the deactivation of the catalyst. Compared with $Pt_{0.3}Sn_{0.6}$/SBA-15, the deactivation rate is slower on Pt_1Sn_2/SBA-15. Based on the

TOF results, it can be seen that the TOF decreases and the stability increases with the increasing of metal loading amount.

According to the results of TEM characterization, the smaller particle size and more homogeneous distribution of PtSn NPs are obtained over $Pt_{0.3}Sn_{0.6}$/SBA-15, $Pt_{0.5}Sn_{1}$/SBA-15 and $Pt_{1}Sn_{2}$/SBA-15 catalysts, which is in favor of improving the catalytic performances due to much more metallic active sites exposed.[49] And with the increasing of Pt and Sn loading amounts, the number of active sites increases. Therefore, the catalytic activity improved for these catalysts with the increasing of Pt and Sn loading. When the loading of Pt increased to 2 wt%, the particle size of PtSn NPs becomes larger and even exceeds 50 nm, which is less active for catalytic reaction. Moreover, there are more oxidative Pt species on $Pt_{2}Sn_{4}$/SBA-15 and $Pt_{3}Sn_{6}$/SBA-15 catalysts, while the Sn species exist in more reduced form than other catalysts. It is reported that the metallic Pt is more active.[50] And the state of Sn species in bimetallic Pt-Sn catalyst also affects the catalytic properties. When Sn exists in a metallic state (Sn^{0}), it may be a poison. When it exists in nonmetallic state (Sn^{n+}), it acts as a promoter. Therefore, $Pt_{2}Sn_{4}$/SBA-15 and $Pt_{3}Sn_{6}$/SBA-15 catalysts with more oxidative Pt and metallic Sn shows non-growth initial conversion of propane, although the loading amounts of Pt and Sn on these catalysts are larger than others. The slow deactivation on these catalysts may also result from the states of Pt and Sn. During the reaction, the Pt species were reduced, which could slow down the deactivation. The reduction speed of Sn species may also be slower than the other catalysts with higher oxidative degree, which is favorable for keeping catalytic performance.

3.3. Coke analysis

3.3.1. Raman spectra

It is well known that coke plays an important role in the catalyst deactivation. Raman spectroscopy is a useful tool to investigate the nature of coke. Figure 10 shows the Raman spectra of PtSn/SBA-15 catalysts after propane dehydrogenation reaction for 6 h. Two Raman bands at around 1600 and 1330 cm^{-1} were observed for PtSn/SBA-15 catalysts. The band at 1600 cm^{-1} is called G band, which is actually the stretching vibration of any pair of sp^2 sites, whether in C=C chains or in aromatic rings. The band at 1330 cm^{-1} is ascribed to D band or disordered band in rings, not in chains.[51] Therefore, these bands provided information not only on the amount of coke formed on the catalyst, but also on its nature. It can be seen that intensity ratio of D and G band over these catalysts are similar, which implies the nature of these catalysts may similar with each other.

3.3.2. O_2-TPO

The TPO profiles of the used catalysts are displayed in Figure 11. It can be seen that two peaks representing different carbon deposits are displayed in TPO profiles. Generally, the carbon deposition corresponding to the first peak at low temperature is mainly the ones that cover the active metal, while the second peak at high temperature represents the ones that located on the external surface of the support. For $Pt_{0.3}Sn_{0.6}$/SBA-15 and $Pt_{0.5}Sn_1$/SBA-15catalysts, it is clear that most of carbon deposits on the support not on the active metal due to the 'drain-off' effect of Sn.[52] With the increasing of Pt content, the intensity of the first peak increases, indicating that more coke which covers the active sites. One reason for this phenomenon is the increasing of the amount of active sites from the increasing of loading amount. The other one is the separation of Pt and Sn on high loading catalysts. The drain-off effect of Sn is weakened on these catalysts. Moreover, the maximal peak temperature of TPO profile shifted to lower temperature, because the Pt is a good catalyst for coke oxidation. With the increasing of Pt content, the catalytic performances for coke oxidation were enhanced for PtSn/SBA-15 catalysts, which result in the shift to low temperature of the high temperature peak.

4. Conclusions

In this work, the PtSn/SBA-15 catalysts with different loading amounts of Pt and Sn were synthesized by simultaneous impregnation of Pt and Sn precursors. The influences of different Pt and Sn loading amounts on the catalyst structure and catalytic performance have been investigated. The high catalytic activity for the propane dehydrogenation has been achieved on Pt_1Sn_2/SBA-15 with propane conversion 54.2% and propene selectivity 98.4%.

In the PtSn/SBA-15 catalyst, the size of PtSn NPs increases with the increasing of Pt and Sn loading, which influences the catalytic performance for propane dehydrogenation. Most importantly, the state of Pt and Sn species changes apparently. The Pt species show more oxidative state and Sn species exhibits more reductive state with the increasing of Pt and Sn loading. This change is unfavourable for the catalytic performance. Therefore, the amounts of the active sites increase due to the increase of Pt and Sn loading amount, but the catalytic performance for propane dehydrogenation shows no improvement when the loading amount of Pt beyond 1 wt%. The loading of Pt and Sn with an appropriate amount is important for balaning the price of catalyst and the catalytic performance.

Acknowledges

The authors are grateful for financial support from National Basic Research Program of China (2012CB215002), Natural Science Foundation of China (21177160, 21376261, 21303263 and 21173270), Beijing Natural Science Foundation (2142027), Doctor select Foundation (20130007110007 and 20130007120011).

References

1 J. J. H. B. Sattler, J. Ruiz-Martinez, E. Santillan-Jimenez and B. M. Weckhuysen, *Chem. Rev.*, 2014, **114**, 10613−10653.

2 A. Ates, C. Hardacre and A. Goguet, *Appl. Catal., A,* 2012, **441**, 30–41.

3 P. Michorczyk, P. Pietrzyk and J. Ogonowski, *Micropor. Mesopor. Mater.,* 2012, **161**, 56–66.

4 F. Ma, S. Chen, H. Zhou, Y. Li and W. Lu, *RSC Adv.*, 2014, **4**, 40776-40781.

5 M. S. Kumar, N. Hammer, M. Rønning, A. Holmen, D. Chen, J. C. Walmsley and G. Øye, *J. Catal.*, 2009, **261**, 116-128.

6 N. S. Gnep, J. Y. Doyemet, A. M. Seco, F. R. Ribeiro and M. Guisnet, *Appl. Catal.,* 1988, **43**, 155-166.

7 R. López Cordero, F. J. Gil Llambias and A. López Agudo, *Appl. Catal.,* 1991, **74**, 125-136.

8 M. E. Harlin, V. M. Niemi, A. O. I. Krause, *J. Catal.*, 2000, **195**, 67-78.

9 J. Salmones, J. A. Wang, J. A. Galicia and G. Aguilar-Rios, *J. Mol. Catal. A*, 2002, **184**, 203–213.

10 L. Nykänen and K. Honkala, *J. Phys. Chem. C,* 2011, **115**, 9578–9586.

11 S. Kaneko, T. Arakawa, M. Ohshima, H. Kurokawa and H. Miura, *Appl. Catal., A,* 2009, **356**, 80–87.

12 I. B. Yarusov, E. V. Zatolokina, N. V. Shitova, A. S. Belyi and N. M. Ostrovskii, *Catal.Today,* 1992, **13**, 655–658.

13 P. Biloen, F. M. Dautzenberg and W. M. H. Sachtler, *J. Catal.,* 1977, **50**, 77–86.

14 S. Gómez-Quero, T. Tsoufis, P. Rudolf, M. Makkee, F. Kapteijn and G. Rothenberg, *Catal. Sci. Technol.,* 2013, **3**, 962–971.

15 Z. Nawaz, X. P. Tang, Y. Wang and F. Wei, *Ind. Eng. Chem.Res.,* 2010, **49**, 1274–1280.

16 J. J. H. B. Sattler, A. M. Beale and B. M. Weckhuysen, *Phys.Chem. Chem. Phys.,* 2013, **15**, 12095–12103.

17 G. Meitzner, G. H. Via, F. W. Lytle, S. C. Fung and J. H. Sinfelt, *J. Phys. Chem.,* 1988, **92**, 2925–2932.

18 H. Verbeek and W. M. H. Sachtler, *J. Catal.,* 1976, **42**, 257–267.

19 J. R. Kitchin, J. K. Norskov, M. A. Barteau and J. G. Chen, *Phys. Rev. Lett.,* 2004, **93**, 156801.

20 W. Z. Lang, C. L. Hu, L. F. Chu and Y. J. Guo, *RSC Adv.,* 2014, **4**, 37107–37113.

21 S. B. He, C. L. Sun, Z. W. Bai, X. H. Dai and B. Wang, *Appl.Catal., A,* 2009, **356**, 88–98.

22 L. Bednarova, C.E. Lyman, E. Rytter and A. Holmen, *J. Catal.*, 2002, **211**, 335–346.

23 J. M. Sun and X. H. Bao, *Chem. Eur. J.,* 2008, **14**, 7478–7488.

24 X. Fan, J. Li, Z. Zhao, Y. Wei, J. Liu, A. Duan and G. Jiang, *Catal. Sci. Technol.,* 2015, **5**, 339-350

25 Y. Uemura, Y. Inada, K. K. Bando, T. Sasaki, N. Kamiuchi, K. Eguchi, A. Yagishita, M. Nomura, M. Tada and Y. Iwasawa, *Phys.Chem. Chem. Phys.,* 2011, **13**, 15833–15844.

26 H. Zhu, D. H. Anjum, Q. Wang, E. Abou-Hamad , L. Emsley, H. Dong, P. Laveille, L. Li, A.K. Samal and J. M. Basset, *J. Catal.,* 2014, **320**,52–62

27 D. Shee and A. Sayari, Appl.Catal., A, 2010, 389, 155–164.

28 D. Y. Zhao, J. L. Feng, Q. S. Huo, N. Melosh, G. H. Fredrickson, B. F. Chmelka and G. D. Stucky, *Science*, 1998, **279**, 548–552.

29 D. Banham, F. Feng, T. Fürstenhaupt, S. Ye and V. Birss, *J. Mater. Chem.,* 2012, **22**, 7164–7171.

30 S. A. Ansari, M. M. Khan, M. O. Ansari, J. Lee and M. H. Cho, *New J. Chem.,* 2014, **38**, 2462-2469.

31 K. Moller and T. Bein, *Chem. Mater.,* 1998, **10**, 2950–2963

32 M. L. Yang, J. Zhu, Y. A. Zhu, Z. J. Sui, Y. D. Yu, X. G. Zhou, D. Chen, *J. Mol. Catal. A,* 2014, **395**, 329-336.

33 M. S. Kumar, D. Chen, J. C. Walmsley, A. Holmen, *Catal. Commun,* 2008, **9**, 747-750.

34 M. L.Yang, Y. A. Zhu, C. Fan, Z.J. Sui, D. Chen and X.G. Zhou, *Phys. Chem. Chem. Phys.,* 2011, **13**, 3257-3267.

35 H. Song, R. M. Rioux, J. D. Hoefelmeyer, R. Komor, K. Niesz, M. Grass, P. Yang and G. A. Somorjai, *J. Am. Chem. Soc.*, 2006, **128**, 3027-3037.

36 Y. Borodko, J. W. Ager III, G. E. Marti, H. Song, K. Niesz and G. A. Somorjai, *J. Phys. Chem. B* 2005, **109**, 17386-17390

37 A. Rahmani, M. Benoit, C. Benoit, *Phys. Rev. B* 2003, **68**, 184202.

38 B. A. Morrow and A. J. McFarlan, *J. Non-Crys. Solids,* 1990, **120**, 61–71

39 J. R. McBride, G. W. Graham, C. R. Peters and W. H. Weber, *J. Appl. Phys.,* 1991, **69**, 1596–1604.

40 W. Lin, A. A. Herzing, C. J. Kiely and I. E. Wachs, *J. Phys. Chem. C* 2008, **112**, 5942-5951

41 A. Leonardy, W. Z. Hung, D. S. Tsai, C. C. Chou and Y. S. Huang, *Cryst. Growth Des.*, 2009, **9**, 3958–3963

42 S. Y. Chen, H. D. Tsai, W. T. Chuang, J. J. Lee, C. Y. Tang, C. Y. Lin and S. Cheng, *J. Phys. Chem. C,* 2009, **113**, 15226–15238

43 X. Yu, J. Li, Y. Wei, Z. Zhao, J. Liu, B. Jin, A. Duan and G. Jiang, *Ind. Eng. Chem. Res.,* 2014, **53**, 9653−9664.

44 X. D. Wang, J. Stöver, V. Zielasek, L. Altmann, K. Thiel, K. Al-Shamery, M. Bäumer, H. Borchert, J. Parisi and J. Kolny-Olesiak, *Langmuir,* 2011, **27**, 11052–11061.

45 B. K. Vu, M. B. Song, I. Y. Ahn, Y. Suh, D. J. Suh, W. Kim, H. Koh, Y. G. Choi and E. W. Shin, *Appl.Catal., A,*2011, **400**, 25–33.

46 Y. Zhang, Y. Zhou, H. Liu, Y. Wang, Y. Xu and P. Wu, *Appl.Catal., A,* 2007, **333**, 202–210.

47 M. Tasbihi, F. Feyzi, M. A. Amlashi, A. Z. Abdullah and A. R. Mohamed, *Fuel Process. Technol.,* 2007, **88**, 883–889.

48 Y. Zhang, Y. Zhou, J. Shi, S. Zhou, Z. Zhang, S. Zhang and M. Guo, *Fuel Process. Technol.,* 2013, **111**, 94–104.

49 X. Liu, W. Z. Lang, L. L. Long, C. L. Hu, L.F. Chu and Y. J. Guo, *Chem. Eng. J.,* 2014, **247**, 183–192

50 S. Sokolov, M. Stoyanova, U. Rodemerck, D.Linke and E. V. Kondratenko, *J.Catal.,* 2012, **293**, 67–75

51 B. M. Vogelaar, A. Dick van Langeveld, S. Eijsbouts and J. A. Moulijn, *Fuel* **2007**, *86*, 1122–1129.

52 H. Lieske, A. Sárkány and J. Völter, *Appl. Catal.,* 1987, **30**, 69–80.

Captions for Tables

Table 1 Textural properties of SBA-15 and supported PtSn/SBA-15 catalysts with different amounts of metal loading.

Table 2 XPS spectra of Pt_{4f} and $Sn3d_{5/2}$ peak analysis results for PtSn/SBA-15 catalysts with different amounts of metal loading.

Table 3 Catalytic performances of propane dehydrogenation over PtSn catalysts supported on SBA-15 and SiO_2

Table 4 The turnover frequencies (TOFs) for the propane dehydrogenation reaction at 5, 30 and 60 min on PtSn/SBA-15 catalysts.

Table 1 Textural properties of SBA-15 and supported PtSn/SBA-15 catalysts with different amounts of metal laoding.

Samples	S_{BET}[a] ($m^2 \cdot g^{-1}$)	V_{mes}[b] ($cm^3 \cdot g^{-1}$)	d_{BJH}[c] (nm)	d_{100}[d] (nm)	a_0[e] (nm)	d_{XRD}[f] (nm)
SBA-15	750.6	1.2	7.8	9.9	11.4	
$Pt_{0.3}Sn_{0.6}$/SBA-15	707.5	1.12	7.4	9.9	11.4	12.8
$Pt_{0.5}Sn_1$/SBA-15	677.4	1.05	7.5	9.9	11.4	21.4
Pt_1Sn_2/SBA-15	650.7	1.04	7.4	9.9	11.4	27.9
Pt_2Sn_4/SBA-15	632.3	1.02	7.5	9.9	11.4	32.6
Pt_3Sn_6/SBA-15	615.6	0.99	7.6	10.1	11.6	38.8

[a] Calculated by the BET method.

[b] The mesoporous volume was calculated using the BJH method.

[c] Mesopore diameter was calculated using the BJH method.

[d] d_{100} is the lattice spacing obtained by low angle XRD.

[e] a_0 is the hexagonal unit-cell parameter calculated using the equation: $a_0 = 2d_{100}/\sqrt{3}$.

[f] d_{XRD} is the average crystallite size evaluated with the Scherrer equation: $d_{hkl}=K(\lambda/\beta)\cos\theta$, where K is the structure constant (0.9 for spherical crystals), λ is the incident ray wavelength (0.154 nm), β is the peak width at half height after correction for instrumental broadening (rad), and θ is the Bragg angle.

Table 2 XPS spectra of Pt_{4f} and $Sn3d_{5/2}$ peak analysis results for PtSn/SBA-15 catalysts with different amounts of metal loading.

Samples	Pt species/%		Sn species/%		
	Pt^0	Pt^{4+}	Sn^0	Sn^{2+},Sn^{4+}	Sn-support
$Pt_{0.3}Sn_{0.6}$/SBA-15	100		4.5	81.2	14.3
$Pt_{0.5}Sn_1$/SBA-15	100		4.1	81.7	14.2
Pt_1Sn_2/SBA-15	91.5	8.5	4.7	84.5	10.8
Pt_2Sn_4/SBA-15	85.9	14.1	4.9	88.2	6.9
Pt_3Sn_6/SBA-15	80.6	19.4	4.8	89.0	6.2

Table 3 Catalytic performances of propane dehydrogenation over PtSn catalysts supported on SBA-15 and SiO_2

Samples	Propane conversion/ %		Propene selectivity/%	
	initial	final[a]	initial	final[a]
SBA-15	0.7	0.6	65.2	65.9
SiO_2	0.2	0.2	47.6	49.6
$Pt_{0.5}Sn_1$/SBA-15	49.5	34.1	98.5	99.1
$Pt_{0.5}Sn_1$/ SiO_2	33.9	19.5	96.9	97.5

[a] Propane dehydrogenation reaction after 6 h.

Table 4 The turnover frequencies (TOFs) for the propane dehydrogenation reaction at 5, 30 and 60 min on PtSn/SBA-15 catalysts.

Samples	Conversion/ % [a]			TOF/ s^{-1} [b]		
	5 min	30 min	60 min	5 min	30 min	60 min
$Pt_{0.3}Sn_{0.6}$/SBA-15	16.1	15.0	14.3	5.88	5.49	5.24
$Pt_{0.5}Sn_1$/SBA-15	20.1	19.1	18.8	5.83	5.55	5.46
Pt_1Sn_2/SBA-15	21.1	20.6	20.1	3.19	3.11	3.04
Pt_2Sn_4/SBA-15	22.0	21.5	20.9	1.91	1.86	1.81
Pt_3Sn_6/SBA-15	21.7	21.1	20.8	1.40	1.36	1.34

[a] Reaction condition: reaction temperature: 500 °C, C_3H_8: 6 ml/min, 0.15 g catalyst.

[b] TOF=molar amount of product/molar amount of Pt metal/s (D=1.13/d)

Captions for Figures

Fig. 1 (A) SAXRD and (B) XRD patterns of SBA-15 and PtSn/SBA-15 catalysts with different amounts of metal laoding: (a) $Pt_{0.3}Sn_{0.6}$/SBA-15, (b) $Pt_{0.5}Sn_1$/SBA-15, (c) Pt_1Sn_2/SBA-15, (d) Pt_2Sn_4/SBA-15, (e) Pt_3Sn_6/SBA-15.

Fig. 2 (A) N_2 adsorption-desorption isotherms and (B) pore size distribution of SBA-15 and PtSn/SBA-15 catalysts with different amounts of metal laoding: (a) $Pt_{0.3}Sn_{0.6}$/SBA-15, (b) $Pt_{0.5}Sn_1$/SBA-15, (c) Pt_1Sn_2/SBA-15, (d) Pt_2Sn_4/SBA-15, (e) Pt_3Sn_6/SBA-15.

Fig. 3 TEM images of (a) SBA-15, (b) $Pt_{0.3}Sn_{0.6}$/SBA-15, (c) $Pt_{0.5}Sn_1$/SBA-15, (d) Pt_1Sn_2/SBA-15, (e) Pt_2Sn_4/SBA-15, (f) Pt_3Sn_6/SBA-15, and (g) HAADF-STEM image and EDS elemental mapping of Pt_3Sn_6/SBA-15.

Fig. 4 Raman spectra of SBA-15 and PtSn/SBA-15 catalysts with different amounts of metal laoding: (a) $Pt_{0.3}Sn_{0.6}$/SBA-15, (b) $Pt_{0.5}Sn_1$/SBA-15, (c) Pt_1Sn_2/SBA-15, (d) Pt_2Sn_4/SBA-15, (e) Pt_3Sn_6/SBA-15.

Fig. 5 UV-Vis DRS spectra of SnO_2 and PtSn/SBA-15 catalysts with different amounts of metal laoding: (a) $Pt_{0.3}Sn_{0.6}$/SBA-15, (b) $Pt_{0.5}Sn_1$/SBA-15, (c) Pt_1Sn_2/SBA-15, (d) Pt_2Sn_4/SBA-15, (e) Pt_3Sn_6/SBA-15.

Fig. 6 XPS spectra corresponding to Pt4f (A) and $Sn3d_{5/2}$ (B) on PtSn/SBA-15 catalysts with different amounts of metal loading: (a) $Pt_{0.3}Sn_{0.6}$/SBA-15, (b) $Pt_{0.5}Sn_1$/SBA-15, (c) Pt_1Sn_2/SBA-15, (d) Pt_2Sn_4/SBA-15, (e) Pt_3Sn_6/SBA-15.

Fig. 7 H_2-TPR profiles of PtSn/SBA-15 catalysts with different amounts of metal loading: (a) $Pt_{0.3}Sn_{0.6}$/SBA-15, (b) $Pt_{0.5}Sn_1$/SBA-15, (c) Pt_1Sn_2/SBA-15, (d) Pt_2Sn_4/SBA-15, (e) Pt_3Sn_6/SBA-15.

Fig. 8 (A) Propane conversion and (B) propene selectivity over PtSn/SBA-15 catalysts with different amounts of metal loading.

Fig. 9 The relationship between catalytic performance and Pt loading amount.

Fig. 10 Raman spectra of the coked catalysts with different amounts of metal loading: (a) $Pt_{0.3}Sn_{0.6}$/SBA-15, (b) $Pt_{0.5}Sn_1$/SBA-15, (c) Pt_1Sn_2/SBA-15, (d) Pt_2Sn_4/SBA-15, (e) Pt_3Sn_6/SBA-15.

Fig. 11 O_2-TPO profiles of the coked PtSn/SBA-15 catalysts with different amounts of metal loading: (a) $Pt_{0.3}Sn_{0.6}$/SBA-15, (b) $Pt_{0.5}Sn_1$/SBA-15, (c) Pt_1Sn_2/SBA-15, (d) Pt_2Sn_4/SBA-15, (e) Pt_3Sn_6/SBA-15.

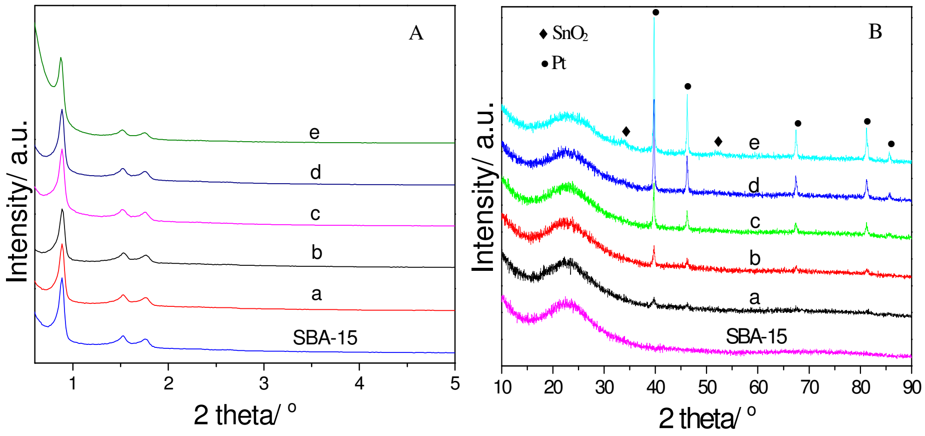

Fig. 1 (A) SAXRD and (B) XRD patterns of SBA-15 and PtSn/SBA-15 catalysts with different amounts of metal laoding: (a) $Pt_{0.3}Sn_{0.6}$/SBA-15, (b) $Pt_{0.5}Sn_1$/SBA-15, (c) Pt_1Sn_2/SBA-15, (d) Pt_2Sn_4/SBA-15, (e) Pt_3Sn_6/SBA-15.

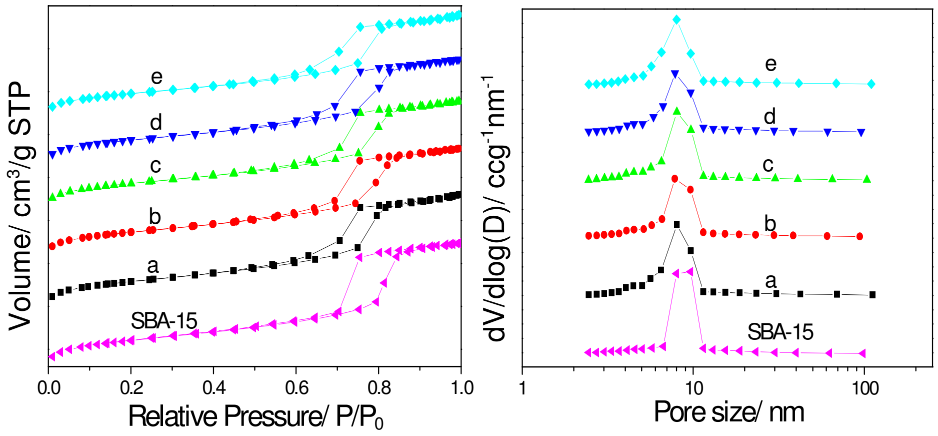

Fig. 2 (A) N_2 adsorption-desorption isotherms and (B) pore size distribution of SBA-15 and PtSn/SBA-15 catalysts with different amounts of metal laoding: (a) $Pt_{0.3}Sn_{0.6}$/SBA-15, (b) $Pt_{0.5}Sn_1$/SBA-15, (c) Pt_1Sn_2/SBA-15, (d) Pt_2Sn_4/SBA-15, (e) Pt_3Sn_6/SBA-15.

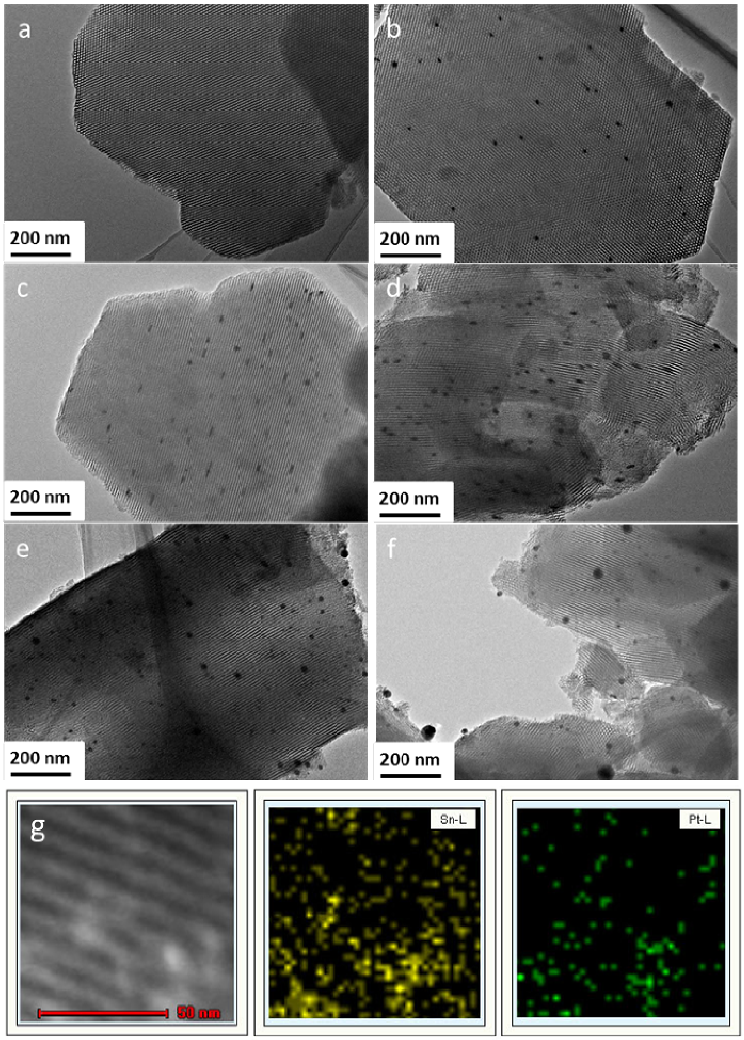

Fig. 3 TEM images of (a) SBA-15, (b) $Pt_{0.3}Sn_{0.6}$/SBA-15, (c) $Pt_{0.5}Sn_{1}$/SBA-15, (d) $Pt_{1}Sn_{2}$/SBA-15, (e) $Pt_{2}Sn_{4}$/SBA-15, (f) $Pt_{3}Sn_{6}$/SBA-15, and (g) HAADF-STEM image and EDS elemental mapping of $Pt_{3}Sn_{6}$/SBA-15.

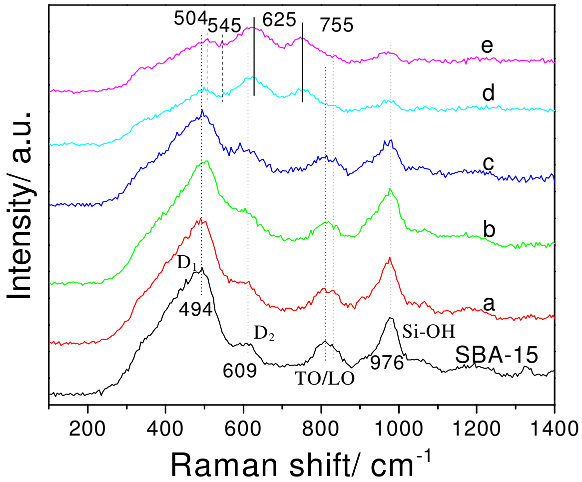

Fig. 4 Raman spectra of SBA-15 and PtSn/SBA-15 catalysts with different amounts of metal laoding: (a) $Pt_{0.3}Sn_{0.6}$/SBA-15, (b) $Pt_{0.5}Sn_1$/SBA-15, (c) Pt_1Sn_2/SBA-15, (d) Pt_2Sn_4/SBA-15, (e) Pt_3Sn_6/SBA-15.

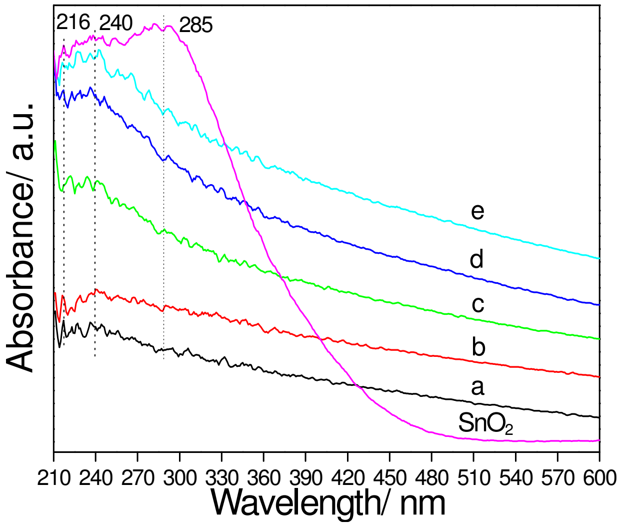

Fig. 5 UV-Vis DRS spectra of SnO_2 and PtSn/SBA-15 catalysts with different amounts of metal laoding: (a) $Pt_{0.3}Sn_{0.6}$/SBA-15, (b) $Pt_{0.5}Sn_1$/SBA-15, (c) Pt_1Sn_2/SBA-15, (d) Pt_2Sn_4/SBA-15, (e) Pt_3Sn_6/SBA-15.

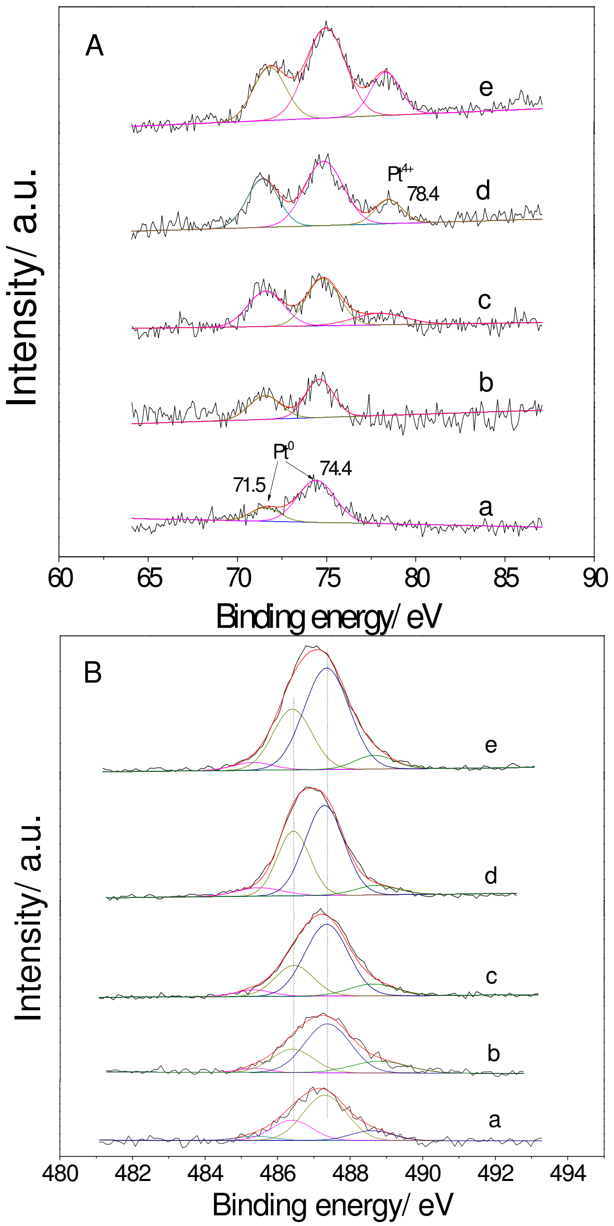

Fig. 6 XPS spectra corresponding to Pt4f (A) and Sn3d$_{5/2}$ (B) on PtSn/SBA-15 catalysts with different amounts of metal loading: (a) Pt$_{0.3}$Sn$_{0.6}$/SBA-15, (b) Pt$_{0.5}$Sn$_{1}$/SBA-15, (c) Pt$_{1}$Sn$_{2}$/SBA-15, (d) Pt$_{2}$Sn$_{4}$/SBA-15, (e) Pt$_{3}$Sn$_{6}$/SBA-15.

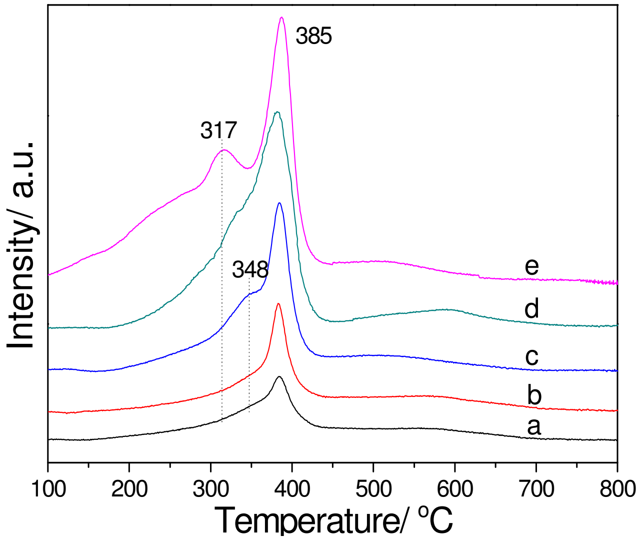

Fig. 7 H_2-TPR profiles of PtSn/SBA-15 catalysts with different amounts of metal loading: (a) $Pt_{0.3}Sn_{0.6}$/SBA-15, (b) $Pt_{0.5}Sn_1$/SBA-15, (c) Pt_1Sn_2/SBA-15, (d) Pt_2Sn_4/SBA-15, (e) Pt_3Sn_6/SBA-15.

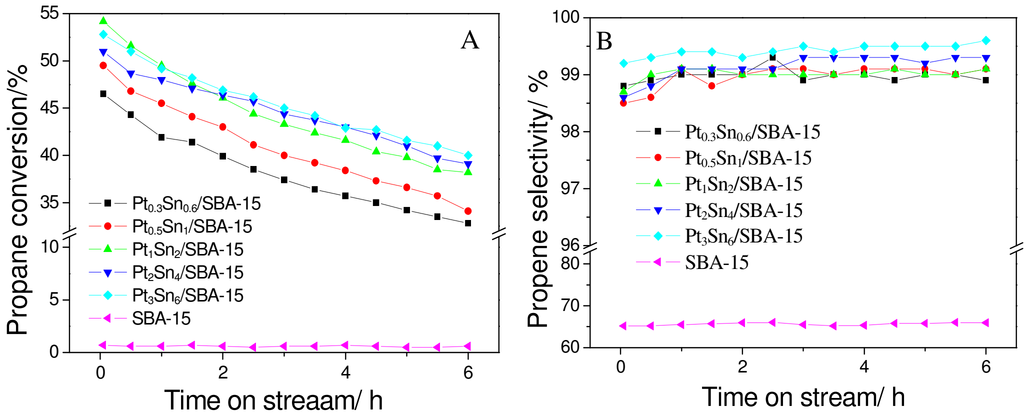

Fig. 8 (A) Propane conversion and (B) propene selectivity over PtSn/SBA-15 catalysts with different amounts of metal loading.

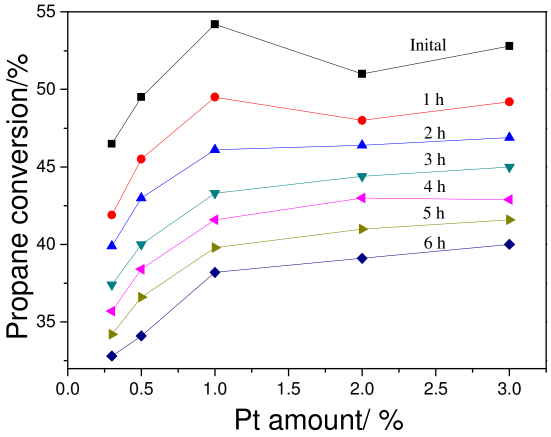

Fig. 9 The relationship between catalytic performance and Pt loading amount.

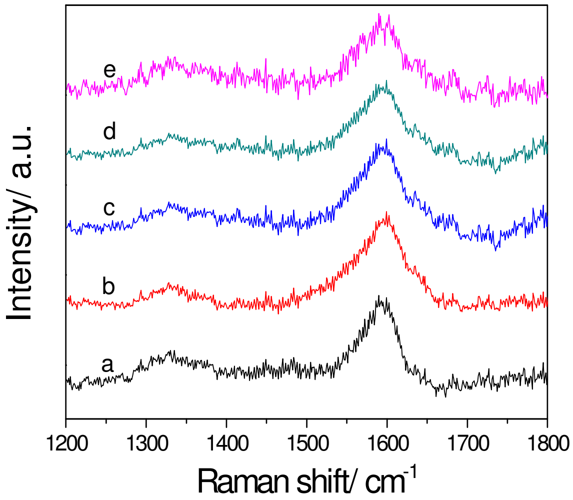

Fig. 10 Raman spectra of the coked catalysts with different amounts of metal loading: (a) $Pt_{0.3}Sn_{0.6}$/SBA-15, (b) $Pt_{0.5}Sn_1$/SBA-15, (c) Pt_1Sn_2/SBA-15, (d) Pt_2Sn_4/SBA-15, (e) Pt_3Sn_6/SBA-15.

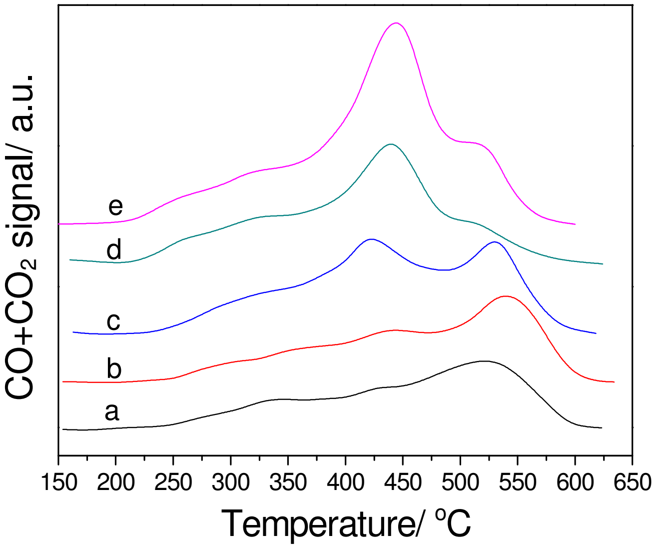

Fig. 11 O$_2$-TPO profiles of the coked PtSn/SBA-15 catalysts with different amounts of metal loading: (a) Pt$_{0.3}$Sn$_{0.6}$/SBA-15, (b) Pt$_{0.5}$Sn$_1$/SBA-15, (c) Pt$_1$Sn$_2$/SBA-15, (d) Pt$_2$Sn$_4$/SBA-15, (e) Pt$_3$Sn$_6$/SBA-15.